Icarus 217 (2012) 194–201

Contents lists available at SciVerse ScienceDirect

Icarus

journal homepage: www.elsevier.com/locate/icarus

# Impact airblast triggers dust avalanches on Mars

Kaylan J. Burleigh [a,*], Henry J. Melosh [b], Livio L. Tornabene [c], Boris Ivanov [a,d], Alfred S. McEwen [a], Ingrid J. Daubar [a]

[a] Lunar and Planetary Laboratory, The University of Arizona, Tucson, AZ 85721, United States
[b] Earth and Atmospheric Sciences, Purdue University, West Lafayette, IN 47907, United States
[c] Center for Earth and Planetary Studies, Smithsonian Institution, Washington, DC 20013, United States
[d] Institute for the Dynamics of the Geospheres, Moscow, Russia

ARTICLE INFO

*Article history:*
Received 17 February 2011
Revised 21 September 2011
Accepted 31 October 2011
Available online 9 November 2011

*Keywords:*
Cratering
Impact processes
Mars, Surface
Meteors

ABSTRACT

Visible images from the Mars Reconnaissance Orbiter have revealed more than 200 new impact sites on Mars (almost all in dust-mantled regions) containing 1–50 m diameter craters, often in clusters. We count approximately 65,000 small-scale slope streaks within 2 to 3 km of one such cluster and categorize them into four morphologically distinct types. Here we show that these slope streaks (interpreted as dust avalanches) are triggered by the impact event but, surprisingly, are not due to seismic shaking; instead, the dust avalanches are due to airblasts created by the supersonic meteor(s) before impact. Sixteen of the new impact sites are associated with high areal densities of dust avalanches. The observed dust avalanche frequency suggests that impact-generated airblasts constitute a locally important and previously unrecognized process for inducing slope degradation on Mars.



## 1. Introduction

The High Resolution Imaging Science Experiment (HiRISE) imaging system (McEwen et al., 2007a,b, 2010) on the Mars Reconnaissance Orbiter (MRO) has re-imaged and confirmed that newly-formed small (1–2 km diameter) dark spots on Mars are the sites of recent (most less than 10 years old) small (<50 m diameter) impact craters or crater clusters (Malin et al., 2006). We refer the reader to Daubar and McEwen (2009), Daubar et al. (2010, 2011a,b), Ivanov et al. (2008, 2009), Kennedy and Malin (2009), Byrne et al. (2009), and McEwen et al. (2007a,b, 2010) for further information on these new impact sites.

At present, more than 200 such impact sites have been confirmed (Daubar et al., 2011b) in images from MRO's Context Imager (CTX; ~5 m/pixel) (Malin et al., 2007) and HiRISE (~0.25 m/pixel) (McEwen et al. 2007a,b). Nearly all of these new impact sites are discovered on dust-mantled regions where impacts clear away or disturb the bright surface dust forming the dark spots we refer to as darkened areas.

## 2. Observations

We analyzed a cluster of five large craters (all formed in one impact event) centered on one of these darkened areas in HiRISE image PSP_002764_1800 (Fig. 1a). At this site the steep dusty slopes are uniformly distributed within and around the darkened area. The largest crater is ~21.7 m in diameter and is located at 226.93°E, 0.03°S. Based on THEMIS (Christensen et al., 2004) and MOC (Malin et al., 1992) observations, this cluster formed between 9 May 2004 and 17 February 2006 (Malin et al., 2006). It is located on the plains of the Amazonian-age Upper Medusae Fossae formation (Scott and Tanaka, 1986) approximately 825 km south of the boundary scarp of Olympus Mons. The impact struck nearly on the boundary between two distinct ridged terrains (Fig. 1a). To the North, ridges (which we interpret at mega-yardangs) are spaced about 375 m apart; to the South, smaller ridges (which we interpret as meso-yardangs) are spaced about 25 m apart. This impact site was re-imaged 226 days later (PSP_005665_1800) and 3.5 years later (ESP_019154_1800), and the surface appears unchanged in both instances. Note, 14 impact sites (including PSP_002764_1800) were imaged before and after the 2007 Mars global dust storm, and only one site showed noticeably different albedo markings (Geissler et al., 2010).

We interpret the thousands of downhill-trending dark streaks on the flanks of mega and meso-yardang ridges as dust avalanches (Sullivan et al., 2001; Baratoux et al., 2006). This interpretation is consistent with HiRISE observations of the topographic relief expected from avalanching (Chuang et al., 2007). Our goal is to determine whether the impact event caused the dust avalanches in PSP_002764_1800, and to discriminate between two possible triggering mechanisms: seismic shaking or airblast-induced slope failure.

* Corresponding author.
*E-mail address:* kaylanb@email.arizona.edu (K.J. Burleigh).

0019-1035/$ - see front matter © 2011 Elsevier Inc. All rights reserved.
doi:10.1016/j.icarus.2011.10.026

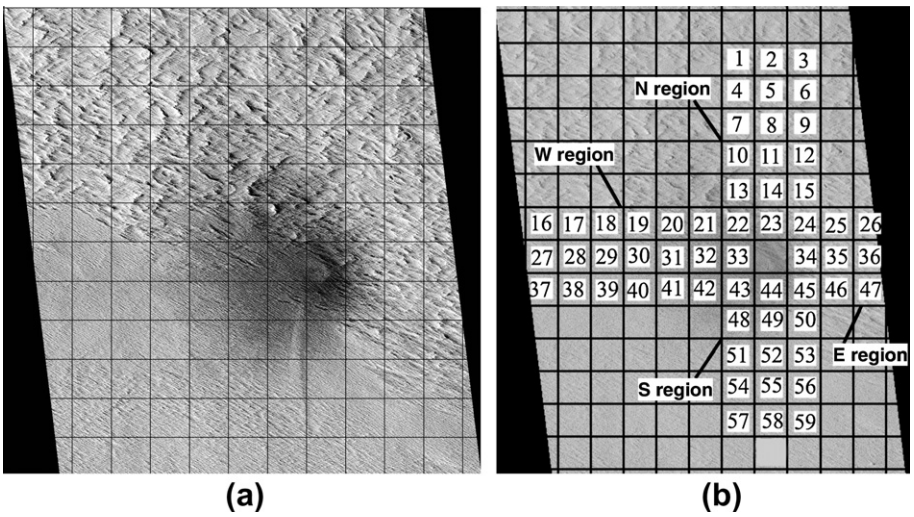


**Fig. 1.** HiRISE image (PSP_002764_1800) and grid system. (a) HiRISE image (PSP_002764_1800). North is up. Notice the central impact site, darkened area, and two distinct terrains: mega-yardangs (middle-top) and meso-yardangs (middle-bottom). (b) Grid system. We count dust avalanches within the 500 × 500 m grid cell system shown. The N, E, S, and W regions are labeled. The eight grid cells surrounding the central impact site (blank grid cell) are assigned to the N, E, S, and W regions as follows: 22, 33, and 43 belong to the W region, 24, 34, and 45 belong to the E region, 23 belongs to the N region, and 44 belongs to the S region.

## 3. Methods

Using the software program Environment for Visualizing Images (ENVI (1998) ENVI Programmer's Guide. Research System, Inc., 930 pp.), version 4.5, we superimposed a 500 × 500 m grid cell system over the image (Fig. 1b) to establish uniform areas for counting dust avalanches.

We grouped grid cells into North (N), South (S), East (E) and West (W) regions (Fig. 1b). These four rectangular regions allow us to: first, count dust avalanches over large contiguous areas as opposed to smaller separated ones; and second, still sample the avalanche distribution in all four cardinal directions away from the impact site. Within each grid, we drew line segments over each dust avalanche to count, classify, locate, and determine its orientation. We bin these data by grid. Distances are measured from the largest crater in the cluster to the geometric center of each grid. Dust avalanche density is calculated by the ratio avalanche number/grid cell area.

## 4. Results

We classified 64,948 avalanches within the grid system. To get this number, we counted over 100,000 avalanches (this includes duplicated counts) because many test counts were required before we could devise a consistent counting technique. Some regions with an apparently discrepant number of counts were also recounted to ensure accuracy. Four types of dust avalanches, designated CL1, CL2, CL4, and CLFaint avalanches, were defined based on their relative albedo and morphology (see Fig. 2a). Type CL1 avalanches are dark with sharply defined edges, longitudinal grooves, and well-defined toes. Type CL2 avalanches have a slightly higher albedo than CL1 avalanches and they lack both longitudinal grooves and well-defined toes. CL2 avalanches also vary in length, from about 3 to 25 m, more than any other avalanche type (see Fig. 2a). Type CL4 avalanches possess degraded margins and a mottled appearance (i.e., they cannot be defined as only bright or only dark streaks). Finally, type CLFaint avalanches have the highest albedo of any avalanche type and appear blurred, faint, and narrow. Note, we do not include the lengths of avalanches in our classification system as length seems to only depend on ridge flank size; albedo and longitudinal grooves are more accurate criteria as these mainly depend on the avalanche morphologies.

The four distinct avalanche types may appear arbitrarily many, but each type is necessary to account for the morphological differences among the observed avalanches (Fig. 2b). Because CL1 avalanches have evident groove markings and a darker albedo than CL2 avalanches (see Fig. 2a), our presumption is that a darker avalanche albedo implies a larger volume of excavated material. Other explanations, such as differences in avalanche age or deposition rates, are also possible. Knowing avalanche type is then a more useful quantity than avalanche surface area.

Due to generally E–W trending ridges, there is a strong terrain bias for N–S dust avalanche orientation (Fig. 2b). Approximately 60% of CL1 and CL2 avalanches are oriented within ±15 degrees of the N–S direction while only 5% are oriented more than 60 degrees from the N–S direction (Fig. 3).

The angular width of each dust avalanche determines the uncertainty in orientation: ±1.4 degrees for CL1, CL4, and CLFaint avalanches (assuming 20 m average length, 0.5 m average width) and between ±1.4 and ±2.0 degrees for CL2 avalanches (assuming average lengths between 7 and 20 m and average widths between 0.3 and 0.5 m). Dust avalanche flow direction is independent of location relative to the impact site; it only depends on dust avalanche type: CL1 avalanches flow S to N, CL2 avalanches flow N to S and S to N, and CL4–CLFaint avalanches flow N to S. In the N region, CL1 avalanches lie on slopes facing away from the impact site (anti-facing) but lie on slopes facing towards the impact site (impact-facing) in the S region. CL2 avalanches lie on impact-facing and anti-facing slopes in both the N and S regions. CL4–CLFaint avalanches lie on impact-facing slopes in the N region and anti-facing slopes in the S region. Illumination, from the W, does not influence streak classification. Avalanche albedo appears to reflect the albedo of the underlying material revealed by the avalanche.

Ridge size controls the average dust avalanche length. The N and E regions lie entirely in the mega-yardang terrain while most of the S and W regions lie in the meso-yardang terrain. In total, 34 grids lie in mega-yardang terrain and the remaining 25 grids lie in meso-yardang terrain. Mega-yardang dust avalanches tend to be nearly twice as long as meso-yardang ones with almost twice as many CL1 avalanches occurring in mega-yardang terrain compared to meso-yardang terrain (see Fig. 4). This suggests CL1 avalanches only form on sufficiently large parent ridge flanks.

We consider CL1 and CL2 avalanches to be dust avalanches created by the impact event. CL1 and CL2 avalanche densities

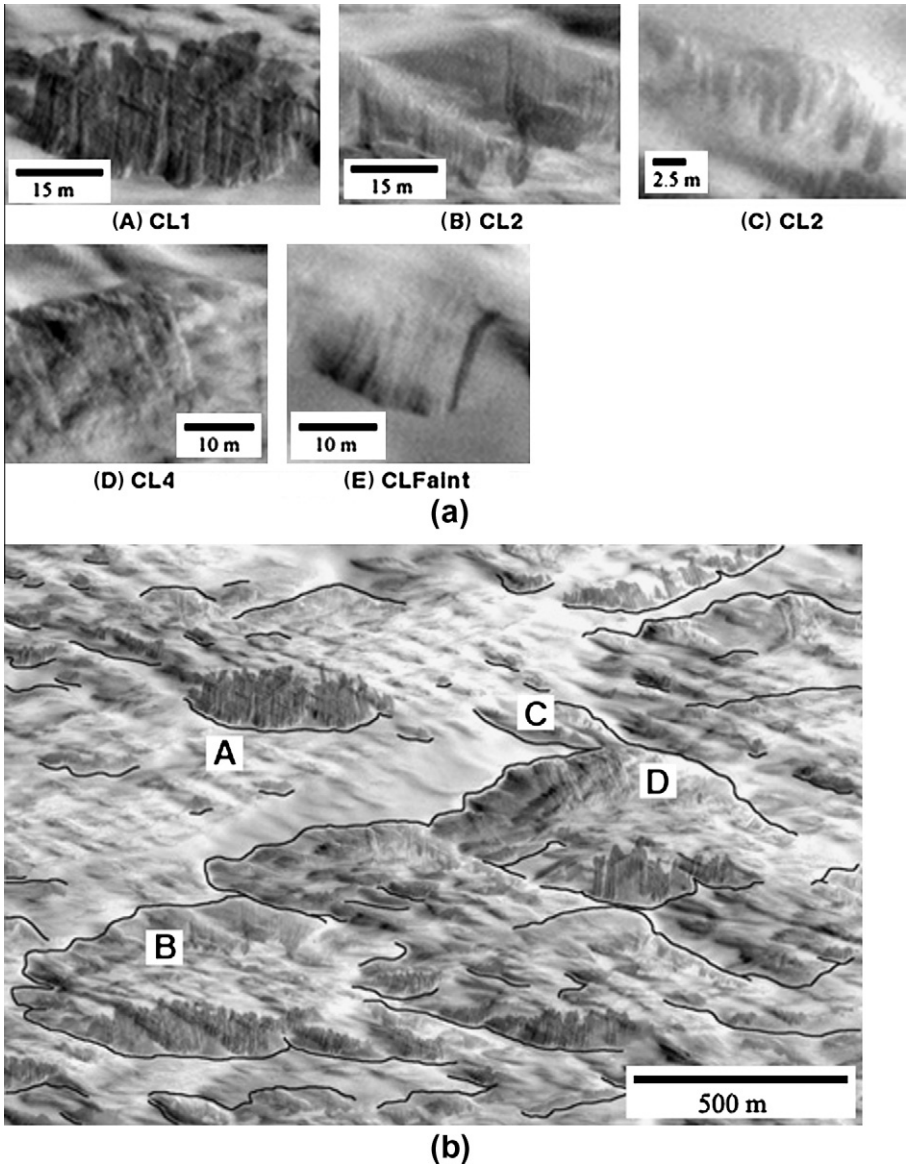


**Fig. 2.** Dust avalanche classification. (a) A, type CL1 avalanches. B and C, type CL2 avalanches. Notice the relatively large range of possible in CL2 avalanche lengths. D, type CL4 avalanches. E, type CLFaint avalanches. (b) Dust avalanche location relative to parent ridge crests. A, B, C, and D come from this image. We infer that avalanche ridge crests, shown here by black curves, are sites of dust avalanche initiation, while avalanche down-slope toes are sites of dust avalanche termination. Ridge crests are revealed when grouping of avalanches appear to start or end (i.e., start) at nearly the same height or position. Down-slope toes are indicated when almost every avalanche in a grouping appears to start or end (i.e., end) at a different height or position.

decrease with distance away from the impact site outside of a dust avalanche-free zone about 500 m in diameter that surrounds the crater cluster (Fig. 5).

This central zone may have been blanketed by impact ejecta that obscures any underlying dust avalanches. The CL1 and CL2 avalanche density distribution traces out a parabola that opens to the West (Fig. 5). The CL1 and CL2 avalanche density decreases at approximately the same rate in the N region as in the S region (Fig. 6a), more gradually in the W region (Fig. 6b), and very sharply in the E region (Fig. 6b).

CL1 and CL2 avalanche density is highest near the impact, reaching a maximum of 9516 $km^{-2}$ in the N region at 0.8 km, 9004 $km^{-2}$ in the E region at 0.5 km, 15,164 $km^{-2}$ in the S region at 1.0 km, and 10,988 $km^{-2}$ in the W region at 1.0 km. The differences between rates of decay in CL1 and CL2 avalanche density among the N, E, S, and W regions imply that the impactor traveled along a W to E trajectory. We suggest a W to E trajectory for the impactor when it may actually have traveled SW to NE or NE to SW. By sampling avalanches in only the cardinal directions, we cannot further constrain the impact trajectory.

We infer that type CL4 and CLFaint avalanches are pre-impact dust avalanches. CL4 avalanches do not appear to correlate with distance from the impact (Fig. 6c), except in the E region (Fig. 6d), while CLFaint increase with distance from the impact (Fig. 6e and f). We directly observe CL1 and CL2 avalanches superimposed on older CL4 avalanches (see Fig. 7). In Fig. 7 the dark CL1 avalanches are in contrast to the brighter CL4 avalanches and surrounding terrain.

This suggests that the CL1 avalanches occurred after the CL4 avalanches formed; however, we cannot know this for sure without a similar image of the region taken before HiRISE image (PSP_002764_1800). CLFaint avalanches strongly anti-correlate with CL1 and CL2 avalanches (Fig. 5). In the N, S, and E regions, CLFaint avalanches approach the same maximum density of about

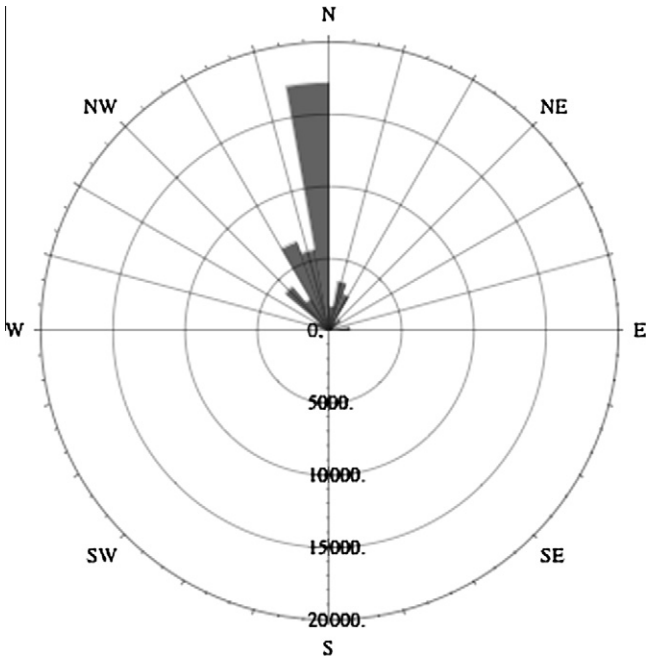


**Fig. 3.** Rose diagram showing the orientation and number of impact induced avalanches, types CL1 and CL2. About 60% of observed CL1 and CL2 avalanches are oriented within ±15 degrees of the N–S direction. Only 5% are oriented more than 60 degrees from the N–S direction.

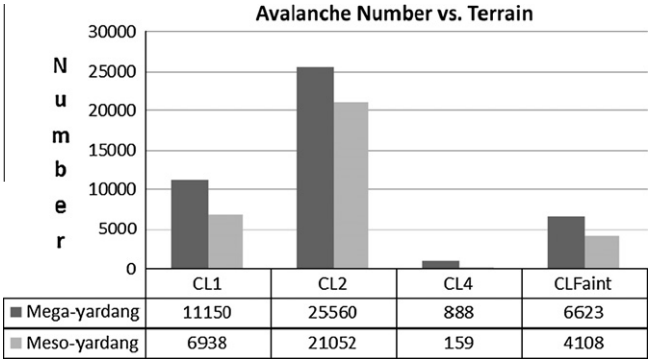


**Fig. 4.** Number of avalanches occurring in mega-yardang versus meso-yardang terrain. The mega-yardang terrain, representing 34 grids, is more spatially extended than the meso-yardang terrain which represents only 25 grids. We expect to find more avalanches in the mega-yardang terrain, but CL1 avalanches tend to be longer and more frequent in the mega-yardang terrain compared to CL1 avalanches in the meso-yardang terrain. This suggests that CL1 avalanches only form on sufficiently large ridge flanks.

3200 km$^{-2}$ (Fig. 6e and f) compared to CL1 and CL2 avalanches which approach minimum densities near 0 km$^{-2}$ at 3.2 km, 2.3 km, and 1.5 km (Fig. 6a and b) in the N, S, and E regions respectively. In the W region, CLFaint avalanches never achieve an appreciable density and the CL1 and CL2 avalanche density never drops below about 3100 km$^{-2}$. We agree with Schorghofer et al.'s (2007) interpretation that bright slope streaks (i.e., CLFaint avalanches and possibly CL4 avalanches) are remnants of dark slope streaks.

A best-fit power law and exponential function were applied to the number density of CL1 and CL2 avalanches versus distance from the largest crater. The best-fit power laws are −2.53 and −2.19 for the N and S quadrants, respectively (excluding the inner 1 km ejecta-blanketed zone on the North and 0.5 km on the South) with a goodness of fit $R$ = 0.90 and 0.75. An exponential decay with

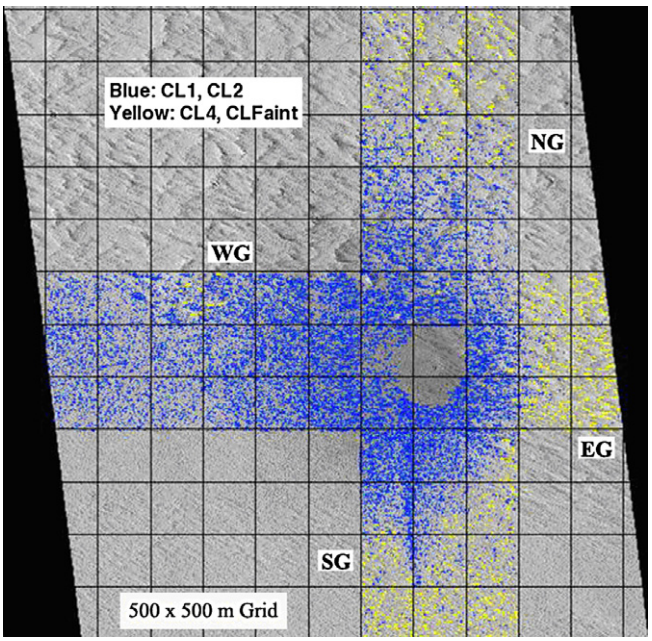


**Fig. 5.** CL1–CL2 and CL4–CLFaint avalanche locations (64,948 dust avalanches shown). The start and end points of every dust avalanche within the N, E, S, and W regions are marked with color coded lines. At this low resolution, these lines appear as dots which show the large scale distribution of dust avalanche densities. The sharp blue–\yellow boundary implies that the decrease in the number of CL1 and CL2 avalanches is correlated with the increase in the number of CL4 and CLFaint avalanches. No dust avalanches appear within approximately 500 m of the impact site. This may be due to mantling by impact ejecta.

distance offers marginally better fits with e-folding distances of 0.81 and 0.60 km, respectively ($R$ = 0.93 and 0.85). The decline to the West is substantially less rapid for either type of fit: −1.1 ($R$ = 0.94) for a power law (excluding the inner 1 km) and e-folding distance of 1.9 km for an exponential decay. In contrast, the dust avalanche density to the East falls off very rapidly, with a power law of −4.5 ($R$ = 0.92) or e-folding distance of 0.24 km ($R$ = 0.90).

## 5. Trigger mechanism

A crucial observation relevant to the trigger mechanism is provided by a narrow, curved, scimitar-shaped, albedo feature (the "Primary Scimitar") that passes through grids 43, 48, 51, 54, and 55 and extends about 2 km South of the impact (see Fig. 8).

The Primary Scimitar is laterally split into a higher albedo West section and a lower albedo East section. It is only composed of CL1 and CL2 avalanches. There is also a much fainter, second scimitar-like feature (the "Secondary Scimitar") that passes through grids 21, 22, and 33 (see Fig. 8). The Secondary Scimitar has similar high and low albedo sections to the Primary Scimitar. The two scimitars are symmetric about a North-Easterly line and exhibit the "parabolic geometry" which Ivanov et al. (2010) describes as due to shock front interactions.

Unlike the impact-induced darkened area around the crater cluster and most other small impacts occurring in dust-mantle regions, the Primary Scimitar's lower albedo East section is due to its exceptionally large density of dust avalanches relative to its surrounding terrain. Conversely, the Primary Scimitar's higher albedo West section is due to its exceptionally low density of dust avalanches. Within the impact's dark spot boundary, approximately 1 km away from the impact, the Primary Scimitar's CL1 and CL2 avalanche density is 16,576 km$^{-2}$ in the lower albedo East section, 11,443 km$^{-2}$ in the higher albedo West section, and 16,431 km$^{-2}$

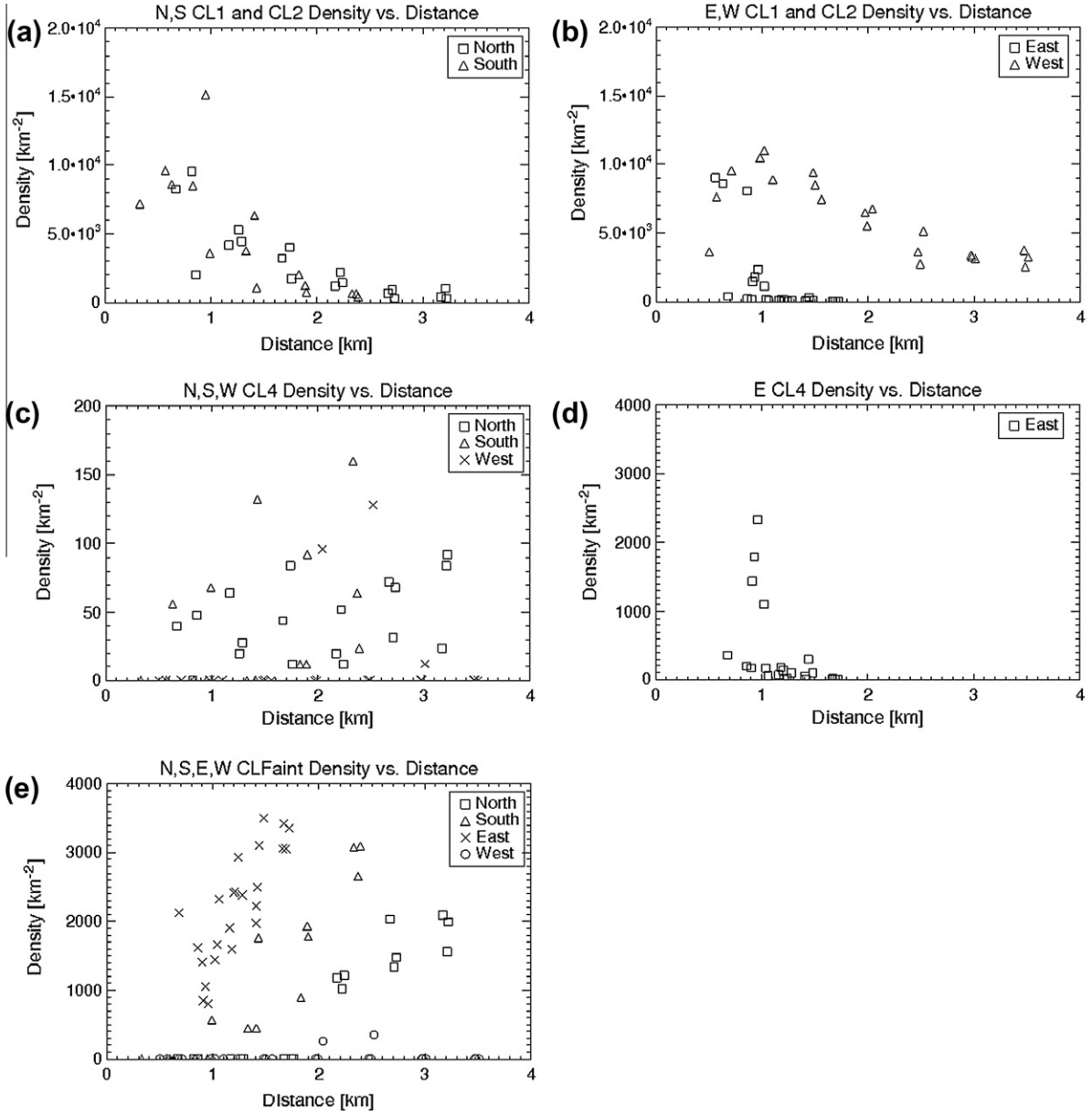


**Fig. 6.** Dust avalanche density versus distance from largest crater. (a) CL1 and CL2 avalanche density versus distance in the N and S regions. CL1 and CL2 avalanche densities decay at a similar rate in the N and S regions. (b) CL1 and CL2 avalanche density versus distance in the E and W regions. CL1 and CL2 avalanche density decreases much faster in the E region than in the W region. (c) CL4 avalanche density versus distance for the N, S, and W regions. The CL4 avalanche densities do not correlate with distance and are much less than nearly all CL1 and CL2 avalanche densities. (d) CL4 avalanche density versus distance for the E region. CL4 avalanche density increases with distance and the maximum CL4 avalanche densities are almost 10 times greater than those in the N, S, and W regions. The E region is plotted separately because CL4 avalanches in the E region have much larger densities than CL4 avalanches in the N, S, and W regions (e) CLFaint avalanche density versus distance for the N, S, and W regions. (f) CLFaint avalanche density versus distance for the E region. CLFaint avalanche densities are too small to show up on the plot at distances less than 1 km from the impact. After 1 km, CLFaint avalanche densities increase with distance and asymptotically approach a maximum density near 3200 km$^{-1}$ in all four regions. Again, the E region is plotted separately because the slope of the E CLFaint avalanche density versus distance curve is much steeper than any of the N, S, and W CLFaint avalanche density versus distance curves.

outside of the Primary Scimitar. Just outside the dark spot, approximately 1.5 km away, the Primary Scimitar's CL1 and CL2 avalanche density is 11,757 km$^{-2}$ in the lower albedo East section, 4470 km$^{-2}$ in the higher albedo West section, and 6120 km$^{-2}$ outside of the Primary Scimitar.

## 6. Discussion

### 6.1. Possible triggering mechanisms

The anti-symmetric density distribution of fresh dust avalanches, types CL1 and CL2, around a site of recent small impacts (Fig. 5) confirms that the impact event triggered the CL1 and CL2 avalanches. The low albedo of CL1 and CL2 avalanches and the impact's dark spot may be due to the exposure of darker underlying materials.

It is most unlikely that seismic waves emanating from the craters could produce the regular bipolar dust avalanche distribution within the scimitars as well as the overall symmetric organization about the impact site itself. Seismic waves due to small-scale explosion cratering in terrestrial environment are well studied experimentally (Cooper and Sauer, 1977). Some experimental data for large-scale avalanche triggering by explosion seismic waves are collected by Adushkin (2006). The combination of these two

**Fig. 7.** CL1 impact induced avalanches (dark streaks) superimposed on CL4 pre-impact avalanches (bright streaks). The CL4 avalanches and the surrounding terrain have nearly the same brightness, while the CL1 avalanches are much darker. This implies the CL1 avalanches formed after the CL4 avalanches.

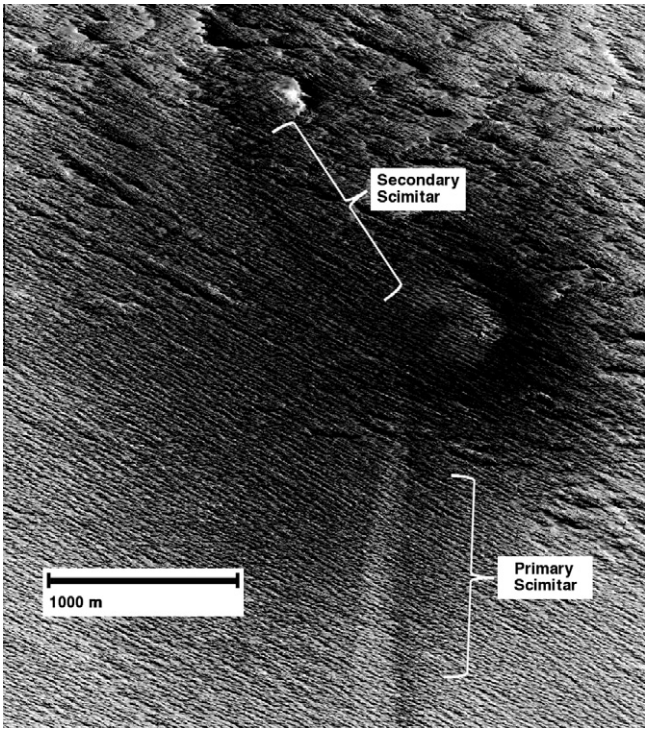


**Fig. 8.** HiRISE image (PSP_002764_1800) stretched (histogram equalization) to better show the Primary and Secondary Scimmitars, as indicated. This Primary and Secondary Scimitars suggest the avalanche trigger mechanism is airblast, not seismic shaking. Such narrow and curved features are unlikely to form from seismic shaking, but can be reproduced by interacting shock fronts (Ivanov et al., 2010).

datasets argue against long-distance triggering ability of near-surface seismic waves propagated away from the cratering point. Although the seismic properties of the martian crust are not well understood (Knapmeyer et al., 2006), short-wavelength seismic waves produced by the impact must attenuate as either 1/r surface waves on an approximately homogeneous layered target (Davis, 1993; Collins et al., 2005) or, if the near-surface of Mars is as chaotically fractured as that of the Moon, as an exponential due to intense scattering (Oberst and Nakamura, 1987). In either case, seismic wave propagation is basically the same in all directions radiating away from the impact site, except as modified by local structure beneath the surface. The observed overall bilateral symmetry of the avalanche distribution and the precise orientation of the scimitars within that pattern are totally at odds with the possibility that seismic scattering created the pattern of avalanche occurrence or avoidance. To argue that the observed pattern is due to seismic scattering would require an extremely unlikely coincidence of a meteoroid impact on a subsurface structure that created nearly identical interference patterns to the North and South of the impact site, while at the same time enhancing propagation to the West and strongly attenuating it to the East, with all these special structures fortuitously centered right on the impact site. If the martian surface were underlain by randomly distributed seismic scattering centers, the pattern of avalanche triggering would create random patches of high and low avalanche densities near the craters that fall off sharply in all directions away from the impact site. The observed pattern is too well organized around the impact site to be plausibly created by seismic scattering from subsurface structures.

Models of airblasts generated by an obliquely traveling supersonic meteorite in the martian atmosphere (Ivanov et al., 2010) reproduce the "parabolic" scimitar-features we observe. The implications of an airblast triggering mechanism for our study are as follows. The Primary Scimitar's shape and width can be explained by the interference between direct and surface-reflected air shocks from the incoming bolide. The higher and lower albedo sections of the scimitars may coincide with shocked regions of "positive and negative pressure" that either elevate material and cause avalanching or indurate material and repress avalanching, respectively. The strong East–West asymmetry, seen in Fig. 5, in Fig. 6b, and in the e-folding distances of 0.24 and 1.9 km for the E and W regions, respectively, is consistent with the airblast produced by an obliquely incident projectile traveling from W to E.

We infer that the dominant triggering mechanism for the dust avalanches was airblast, not seismic shaking. It has already been shown that slope streaks can have relatively large sediment transport rates (Phillips et al., 2007). Impact-generated airblasts causing tens of thousands of avalanches (or slope streaks) may constitute a locally important and previously unrecognized process for slope degradation on Mars.

### 6.2. Avalanche observations at all new impact sites

We looked at the 201 known and dated small impact sites (Daubar et al., 2011a,b) to estimate the global importance of the airblast-avalanching process for Mars. The goal was to determine: One, whether dust avalanches are present; and two, whether favorable conditions for avalanching exist (i.e., adequate dust mantling and steep slopes). We visually inspected each impact site to qualitatively estimate the number of avalanches (i.e., none, few, or many) and checked for the presence of steep slopes from the surface morphology (at 25 cm/pixel, HiRISE). To determine the presence of an appreciable dust mantle, we used a value of the TES dust index < 0.94 (Ruff and Christensen, 2002), thermal inertia < 100 (Christensen et al., 2001; Fergason et al., 2006), as well as a visual inspection of the surface morphology over the nearby area. To find the thermal inertia and TES dust index values, we averaged over the HiRISE footprint using JMARS software (Christensen et al., 2007).

Nearly all 201 sites have at least a thin covering of high-albedo dust, since the clearing of that dust is how they are being discovered. We find that 140 of the new impact sites have both steep slopes and appreciable dusty mantling. Of these, 47 sites contain avalanches, while only 16 sites (including the site we study in this work) contain a large number of dust avalanches (~11% of those sites with conditions favorable for avalanches). Table 1 lists the image numbers and locations for these 16 sites. The impact sites in Table 1 are characterized by a relatively thick dust covering and steep slopes. In some cases, the darkened areas appear to coincide with regions of highest avalanche density. We cannot conclude whether the observed avalanches were all directly caused by the

**Table 1**
Known new impact sites with large numbers of dust avalanches.

| HiRISE observation ID | Latitude (North, planetocentric) | Longitude (East) |
|---|---|---|
| ESP_012588_1855 | 5.31 | 205.78 |
| ESP_013287_1845 | 4.43 | 201.41 |
| ESP_016161_1755 | −4.22 | 220.55 |
| ESP_016465_1735 | −6.42 | 202.40 |
| ESP_016676_1785 | −1.49 | 200.63 |
| ESP_017097_1780 | −1.78 | 227.47 |
| ESP_018561_1710 | −8.88 | 217.64 |
| ESP_020592_1785 | −1.55 | 208.01 |
| PSP_002764_1800 | −0.03 | 226.91 |
| PSP_003602_2085 | 28.46 | 25.20 |
| PSP_003674_1855 | 5.36 | 223.33 |
| PSP_004030_1855 | 5.47 | 224.35 |
| PSP_004123_1915 | 11.37 | 203.51 |
| PSP_005666_1790 | −0.75 | 200.07 |
| PSP_005942_1825 | 2.48 | 224.11 |
| PSP_006998_2060 | 25.61 | 188.59 |

impact itself without a more detailed study. However, the co-location of the avalanches and the impacts suggests causation.

### 6.3. Conclusions

The total area over which the avalanches extended (approximately $10^6$ times larger than the craters themselves) in HiRISE image PSP_002764_1800 suggests that surface modification by small impacts might be more important than previously thought, at least for dust-mantled regions with steep slopes. We use the Pi Scaling method (Melosh, 1989) to estimate that the crater cluster was caused by an impactor about 1 m in diameter. This assumes a "gravity-dominated" crater diameter of 25 to 30 m and a spherical projectile with impact velocity of 7 km/s and impact angle of 45°. Assuming a Martian cratering rate of $1 \times 10^{-6}$ impacts/yr/km$^2$ producing craters larger than 3 m in diameter (Daubar et al., 2011b), and a $2 \times 2$ km CL1 and CL2 avalanche region, every $2 \times 2$ km region on Mars should experience nearly four impacts every 1 million years.

Of the 201 known impact sites, only 16 sites have very high populations of dust avalanches. These 16 sites are all in regions characterized by steep slopes and a relatively high level of dust mantling. Given that new impacts are only being detected in the dustiest regions of Mars, we estimate only 4% of all meter-scale impacts may cause surface degradation by avalanching. It is also possible that smaller avalanches are present, not resolvable by HiRISE. These unresolved avalanches might then be numerous enough to contribute to, or even cause, the low-albedo areas around the new impact sites. Immediately adjacent to the impact site, steep slopes may not even be required for avalanching.

There is no evidence that impact-induced seismic shaking triggered the observed dust avalanches in HiRISE image PSP_002764_1800. Seismic waves should propagate radially away from the impact site, but avalanche distribution about the impact site is anti-symmetric. Seismic waves could scatter around local subsurface structure and possibly produce regions of high and low avalanche density (i.e., if only one scimitar were observed); however, producing the bipolar dust avalanche distribution for the two scimitars would be highly unlikely. Models of airblasts generated by obliquely traveling supersonic meteorites can reproduce the avalanche distributions around the impact site and within the scimitars. We infer that the dominant triggering mechanism for the dust avalanches was airblast, not seismic shaking.

A search for small craters in more rocky or indurated formations with stronger seismic coupling might reveal evidence for seismic triggering; however, the absence of dark halos around small craters in regions lacking a thick dust cover makes it difficult to identify recent craters in terrain more likely to show the effects of seismic triggering.

## Acknowledgments

H.J.M. and B.I. were supported by NASA grant NNX08AM21G. We thank the Icarus reviewers for constructive comments, especially for encouraging analysis of the fainter but very important Secondary Scimitar. We also thank the MRO project for characterization of the new impacts.

## References

Adushkin, V.V., 2006. Landslides from massive rock slope failure. In: Evans, S.G., Mugnozza, G.S., Strom, A., Hermanns, R.L. (Eds.), NATO Science Series IV: Earth and Environmental Sciences, vol. 49. Springer Science + Business media, New York, pp. 267–284.
Baratoux, D. et al., 2006. The role of wind-transported dust in slope streaks activity: Evidence from the HRSC data. Icarus 183, 30–45.
Byrne, S. et al., 2009. Distribution of mid-latitude ground ice on Mars from new impact craters. Science 325, 1674–1676.
Christensen, P.R. et al., 2001. Mars global surveyor Thermal Emission Spectrometer experiment: Investigation description and surface science results. J. Geophys. Res. 106, 23.
Christensen, P.R. et al., 2004. The Thermal Emission Imaging System (THEMIS) for the Mars 2001 Odyssey Mission. Space Sci. Rev. 110, 85–130.
Christensen, P.R., Gorelick, N., Anwar, S., Dickenshied, S., Edwards, C., Engle, E. 2007. New insights about Mars from the creation and analysis of Mars global datasets. Proc. Am. Geophys. Union (fall meeting). Abstract P11E-01.
Chuang, F.C., Beyer, R.A., McEwen, A.S., Thomson, B.J., 2007. HiRISE observations of slope streaks on Mars. Geophys. Res. Lett. 34, 6.
Collins, G.S., Melosh, H.J., Marcus, R.A., 2005. Earth impacts effects program: A web-based computer program for calculating the regional environmental consequences of a meteoroid impact on Earth. Met. Planet. Sci. 40, 817–840.
Cooper, H.F., Sauer, F.M., 1977. Crater-related ground motions and implications for crater scaling. In: Roddy, D.J., Pepin, R.O., Merrill, R.B. (Eds.), Impact and Explosion Cratering: Planetary and Terrestrial Implications. Pergamon Press, New York, pp. 1133–1163.
Daubar, I.J., McEwen, A.S., 2009. Depth to diameter ratios of recent primary impact craters on Mars. Lunar Planet. Sci. XL. Abstract 2419.
Daubar, I.J., McEwen, A.S., Byrne, S., Dundas, C.M., Kennedy, M., Ivanov, B.A., 2010. The current martian cratering rate. Lunar Planet. Sci. XLI. Abstract 1978.
Daubar, I.J. et al., 2011a. New craters on Mars and the Moon. Lunar Planet. Sci. XLII. Abstract 2232.
Daubar, I.J., McEwen, A.S., Byrne, S., Kennedy, M., 2011b. The current martian crater production function. Eur. Planet. Sci. Cong. – Am. Astron. Soc. Abstract 1649.
Davis, P.M., 1993. Meteoroid impacts as seismic sources on Mars. Icarus 105, 469–478.
Fergason, R.L., Christensen, P.R., Kieffer, H.H., 2006. High resolution thermal inertia derived from THEMIS: Thermal model and applications. J. Geophys. Res. 111, 22.
Geissler, P.E., Daubar, I.J., McEwen, A.S., Bridges, N.T., Dundas, C.M., 2010. Eolian degradation of young martian craters. Lunar Planet. Sci. XLII. Abstract 2591.
Ivanov, B.A., Melosh, H.J., McEwen, A.S., HiRISE Team, 2008. Small impact crater clusters in high resolution HiRISE images. Lunar Planet. Sci. XXXIX. Abstract 1221.
Ivanov, B.A., Melosh, H.J., McEwen, A.S., HiRISE Team, 2009. Small impact crater clusters in high resolution HiRISE images – II. Lunar Planet. Sci. XL. Abstract 1410.
Ivanov, B.A., Melosh, H.J., McEwen, A.S., HiRISE Team, 2010. New small impact craters in high resolution HiRISE images – III. Lunar Planet. Sci. XLI. Abstract 2020.
Kennedy, M.R., Malin, M.C. 2009. 100 New impact crater sites found on Mars. Proc. Am. Geophys. Union (fall meeting). Abstract P43D-1455.
Knapmeyer, M., Oberst, J., Hauber, E., Wahlisch, M., Deuchler, C., Wagner, R., 2006. Working models for spatial distribution and level of Mars' seismicity. J. Geophys. Res. 111, 23.
Malin, M.C. et al., 1992. Mars Observor camera. J. Geophys. Res. 97, 20.
Malin, M.C., Edgett, K.S., Posiolova, L.V., McColley, S.M., Noe Dobrea, E.Z., 2006. Present-day impact cratering rate and contemporary gully activity on Mars. Science 314, 1528–1529.
Malin, M.C. et al., 2007. Context camera investigation on board the Mars reconnaissance orbiter. J. Geophys. Res. 112, 25.
McEwen, A.S. et al., 2007a. Mars reconnaissance orbiter's high resolution imaging science experiment (HiRISE). J. Geophys. Res. 112, 40.
McEwen, A.S., Tornabene, L.L., HiRISE Team, 2007b. Modern mars: HiRISE observations of small, recent impact craters. Lunar Planet. Sci. XXXVII. Abstract 3086.
McEwen, A.S. et al., 2010. The high resolution imaging science experiment (HiRISE) in MRO's primary science phase (PSP). Icarus 205, 2–37.
Melosh, H.J., 1989. Scaling of crater dimensions. In: Impact Cratering: A Geological Process. Oxford Univ. Press, New York, pp. 112–125.

Oberst, J., Nakamura, Y., 1987. Distinct meteoroid families identified on the lunar seismograms. J. Geophys. Res. 92, 769–773.
Phillips, C.B., Burr, D.M., Beyer, R.A., 2007. Mass movement within a slope streak on Mars. Geophys. Res. Lett. 34, 5.
Ruff, S.W., Christensen, P.R., 2002. Bright and dark regions on Mars: Particle size and mineralogical characteristics based on Thermal Emission Spectrometer data. J. Geophys. Res. 107, 22.
Schorghofer, N., Aharonson, O., Gerstell, M.F., Tatsumi, I., 2007. Three decades of slope streak activity on Mars. Icarus 191, 132–140.
Scott, D.H., Tanaka, K.L. 1986. Map showing lava flows in the southwest part of the tharsis quadrangle of Mars. USGS Map I-1802-A.
Sullivan, R., Thomas, P., Veverka, J., Malin, M.C., Edgett, K.S., 2001. Mass movement slope streaks imaged by the Mars orbiter camera. J. Geophys. Res. 106, 607–633.